Energy 170 (2019) 14–21

Contents lists available at ScienceDirect

Energy

journal homepage: www.elsevier.com/locate/energy

Visualization of liquid water in a lung-inspired flow-field based polymer electrolyte membrane fuel cell via neutron radiography

J.I.S. Cho [a, b], T.P. Neville [b], P. Trogadas [a], Q. Meyer [b], Yunsong Wu [b], R. Ziesche [b], P. Boillat [c, d], M. Cochet [c], V. Manzi-Orezzoli [c], P. Shearing [b], D.J.L. Brett [a, b], M.-O. Coppens [a, *]

[a] EPSRC "Frontier Engineering" Centre for Nature Inspired Engineering & Department of Chemical Engineering, University College London, London, WC1E 7JE, UK
[b] Electrochemical Innovation Lab, Department of Chemical Engineering, University College London, London, WC1E 7JE, UK
[c] Electrochemistry Laboratory (LEC), Paul Scherrer Institute (PSI), 5232, Villigen, Switzerland
[d] Neutron Imaging and Activation Group (NIAG), Paul Scherrer Institute (PSI), 5232, Villigen, Switzerland

ARTICLE INFO

Article history:
Received 10 August 2018
Received in revised form
14 December 2018
Accepted 18 December 2018
Available online 19 December 2018

Keywords:
Lung-inspired flow-field
Fractal flow-field
Neutron imaging
Flooding
Water management
Fuel cells

ABSTRACT

Lung-inspired, fractal flow-fields hold great potential in improving the performance of polymer electrolyte membrane fuel cells (PEMFCs) by providing uniform gas distribution across the electrodes and ensuring minimum entropy production in the whole system. However, the inherent susceptibility of the fractal flow-fields to flooding renders their use inadequate at high humidity conditions. In-depth understanding of water management in lung-inspired flow-fields is indispensable for the implementation of alternative outlet channel geometries or engineered water removal strategies to alleviate flooding. Here, liquid water formation and transport across the lung-inspired and serpentine flow-field based PEMFCs are evaluated using neutron radiography. The results reveal a propensity to flooding in the interdigitated outlet channels of the fractal flow-field with $N = 4$ generations as a result of slow gas velocity and narrow channel dimensions, which leads to significant performance deterioration. Neutron images also elucidate the importance of ensuring a well-defined internal channel structure of the fractal flow-fields to prevent backflow of liquid water *via* wicking and capillary pressure build-up arising from the narrow inlet gas channels and hydrophobic gas diffusion layer.

1. Introduction

Proton exchange membrane fuel cells (PEMFCs) are one of the most promising alternatives to internal combustion engines and for a wide range of stationary and portable applications [1]. PEMFCs convert the chemical energy of reactants directly into electrical energy by exploiting the electrochemical potential difference arising from two spontaneous half-cell reactions at the electrodes [2]. Water, which is the product of these electrochemical reactions, has to be continuously removed during fuel cell operation to ensure effective reactant transport to the catalyst layer.

One of the long-standing challenges for efficient and reliable fuel cell performance is accomplishing uniform reactant distribution across each electrode. By virtue of the planar geometry of the membrane electrode assembly (MEA), it is customary to distribute reactants in a 2D or quasi-3D fashion using flow-fields [3–9]. However, such approach leads to depletion of reactant concentration along the flow path of the flow-field, rendering gas distribution highly non-uniform [8,10–14]. Such mass transport issue can lead to a series of events [7] detrimental to fuel cell performance [15–17] and longevity [17–19]. This is an inevitable side effect within the confines of the conventional (serpentine, interdigitated, parallel) and bio-imitating designs [8,20–24].

Recently, a lung-inspired flow-field design was proposed by some of the authors that draws inspiration from the fractal geometry and associated functionality of the upper respiratory tract of the human lung (Fig. 1) [25]. This lung-inspired flow-field features three-dimensional fractal branching structures as inlets, delivering uniform reactant distribution across the electrode. The concept of lung-inspired flow-fields was numerically validated, and

* Corresponding author.
E-mail address: m.coppens@ucl.ac.uk (M.-O. Coppens).

https://doi.org/10.1016/j.energy.2018.12.143

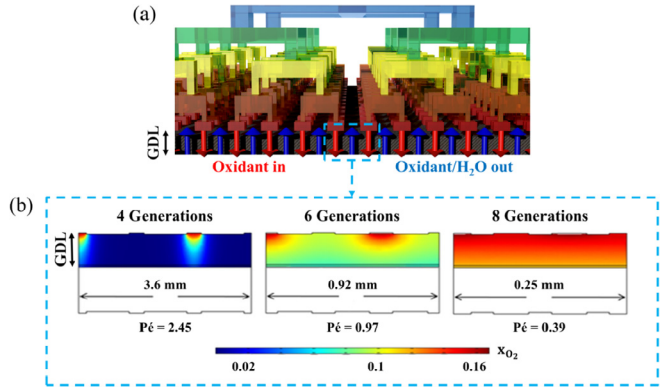

Fig. 1. (a) A computer generated image of the GDL integrated with a fractal flow-field with $N = 4$ branching generations, and (b) numerical simulations conducted in our previous study, illustrating oxygen mass fraction distribution in the cathode catalyst layer using fractal flow-fields with $N = 4$, 6, and 8 generations [16].

the number of branching generations (N) was found to be the key parameter for reactant uniformity. However, these lung-inspired flow-fields are susceptible to flooding under high humidity conditions, especially at high generation numbers (*e.g.*, $N > 4$ for a 10 cm^2 flow-field), where the channels become very narrow, due to slow gas flow across each channel [25].

In contrast to conventional flow-fields, understanding the dynamics of liquid water in lung-inspired flow-fields is limited, partly due to the inherent difficulty in accessing liquid water through the 3D printed stainless steel structure with complex internal channel networks. In-depth understanding of the two-phase flow across the lung-inspired flow-field channels would serve to identify the shortcomings of the current design pertaining to water management and improve it *via* an alternative outlet channel geometry or implementation of an engineered water management strategy.

Thus far, experimental techniques, such as optical [26–28], X-ray tomography [29,30], X-ray radiography [31,32], neutron radiography [33–35], and magnetic resonance imaging (MRI) [36–38], have been employed for *in situ* visualization of liquid water in PEMFCs. Recently, it was revealed *via* neutron radiography that cathode channels of a PEMFC stack with serpentine flow fields have a much larger effect on the water content in the fuel cell and its overall performance than the anode channels [39–43]. Neutron radiography has proven to be a particularly versatile tool in fuel cell research, as it provides information that is inaccessible by any other measurement technique [43,44]. The unique aspects of fuel cell imaging using neutron radiography are due to the high sensitivity to liquid water and good penetration depth through fuel cell components [45]. These traits are crucial to assess the effect of different flow-field designs and operating conditions on liquid water transport and distribution across the electrode [43,46,47].

In this study, through-plane neutron imaging results are presented for the lung-inspired flow-field with $N = 4$ generations, and compared to results for a conventional double-serpentine flow-field. The innovative aspect of the present work lies not only in the design, fabrication method and underlying nature-inspired concept, but, most importantly, in the experimental technique used to visualize transient liquid water generation and transport across the channels of the fractal flow-field. The fuel cell is operated at ambient temperature in the absence of gas humidification. A series of galvanostatic measurements are performed and the corresponding transient changes in fuel cell potential are presented along with neutron images to investigate the effect of liquid water formation and transport on fuel cell performance.

2. Experimental

2.1. MEA fabrication

A 10 cm^2 MEA was fabricated in-house by hot pressing a Nafion 212 membrane (DuPont, USA) and ELE0070 gas diffusion electrodes (Johnson Matthey, UK) using a 12-ton thermal press (Carver, 4122CE). The membrane was used without any pre-treatment, and the assembly was pressed at 130 °C for 3 min with an applied pressure of 400 psi [48]. The membrane has a thickness of 50 μm, and the catalyst layers have a platinum loading of 0.4 mg Pt cm^{-2}.

2.2. PEMFC components

Fig. 2 shows an exploded view of a PEMFC using a lung-inspired flow-field at the cathode. Both end-plates were made of 8 mm thick aluminium plates, which were electroless plated in gold to prevent corrosion. The fractal flow-field used in this study were fabricated in a previous study using 3D printing *via* direct metal laser sintering (DMLS) [25]. The fractal flow-field consists of 3D network of branching inlet channels and interdigitated outlet channels, which are connected by a manifold (Fig. 4). The flow-field was electroplated in-house in gold (Spa Plating, UK) to 1 μm thickness. A detailed description of the dimensions and configuration of the plates and gold electroplating procedure is outlined elsewhere [25]. The fractal flow-field was assembled in the cathode of a PEMFC, in which notable transport limitations occur. A 2 mm thick gold-coated aluminium plate was used as a cathode current collector for the lung-inspired flow-field and a 0.8 mm thick graphite sheet (RS pro, UK) was placed in between for a gas-tight seal. The current collector was used only for the fractal flow-field. Current was drawn directly from the serpentine flow-fields at the anode and cathode. At the anode, a single-channel serpentine flow-field was used with channel width, spacing, and depth of 1 mm, 1 mm, and 0.7 mm, respectively. The anodic serpentine flow-field was made of a 2 mm thick aluminium plate, which was electroless plated in gold.

The behaviour of the above-mentioned setup was compared to a PEMFC using a serpentine flow-field at the cathode. The cathodic double-serpentine flow-field was fabricated by milling channels into a 1.6 mm thick printed circuit board (PCB) plate (35 μm copper layer) to achieve channel width and spacing of 1 mm, and depth of 0.8 mm. At the anode, again, a single-serpentine flow-field was used with channel width, spacing, and depth of 1 mm, 1 mm, and 0.7 mm, respectively. The anodic flow-field was made of a 0.8 mm thick PCB plate (35 μm copper layer). The PCB flow-fields were electroplated to 0.5 μm in nickel (Balco Engineering, UK) and 5 μm in gold (Spa Plating, UK). A 70 μm thick sheet of Tygaflor was used as a gasket at the interface between flow-fields/current collector and end-plates for electrical insulation. The same material was used as a gasket to seal the perimeter of the MEA.

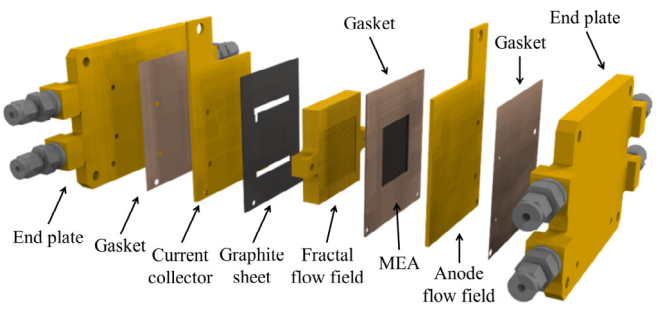

Fig. 2. Exploded view of individual PEMFC components used in this study.

2.3. PEMFC operation

A simplified schematic of the experimental setup is displayed in Fig. 3. The test station supplied dry hydrogen (purity 99.995%) and air at a stoichiometric ratio of 1.2 and 3, respectively, by controlling the gas flow rate using mass flow controllers (EL-FLOW, Bronkhorst). The current drawn from the cell was regulated using a DC electronic load (PLZ664WA, Kikusui). An in-house computer controlled system (LabVIEW, National Instruments) controls the components of the rig and records data with a data acquisition card (USB 6363, National Instruments). The PEMFC was operated without external heating. Table 1 lists the key operating conditions used in all experiments. These conditions were chosen to reproduce a regime of operation expected to be limited by flooding, while preventing condensation in the fractal distribution network, which could otherwise obstruct the through-plane view.

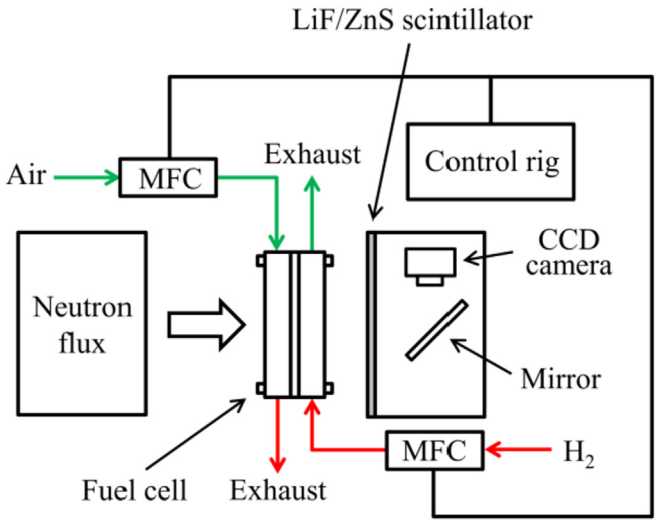

Fig. 3. Simplified schematic for through-plane fuel cell imaging in NEUTRA, facing the LiF/ZnS scintillator [49]. MFC stands for mass flow controller.

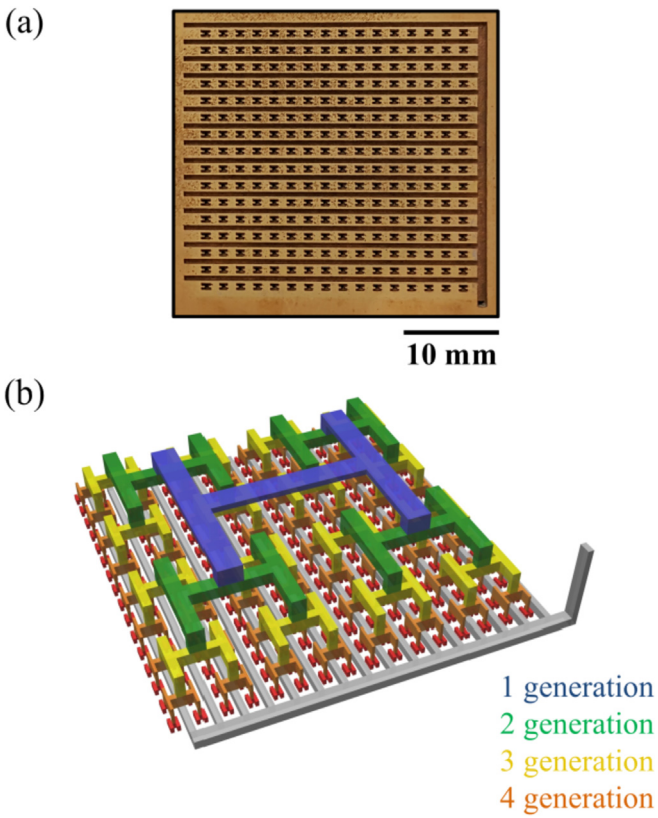

Fig. 4. (a) Optical image of the gold plated engineered flow-field with $N = 4$ generations showing fractal inlet and interdigitated outlet channels and (b) a schematic showing the fractal geometry. The fractal flow-fields comprise self-similar, repeatedly branching "H" shaped channels designed to uniformly distribute reactant across the catalyst layer surface. This channel geometry allows a single inlet to branch into 4^N outlets with each flow path being equal in length.

Table 1
Operating conditions used during PEMFC operation.

Parameter	Value
Fuel cell temperature	Ambient
Cathode RH	Dry
Anode RH	Dry
Hydrogen stoichiometry (α_{H2})	1.2
Air stoichiometry (α_{air})	3
Active area	10 cm^2
Membrane	Nafion 212
Electrode	ELE0070
Cathode/anode outlet pressure	1 atm (abs)

Experiments were conducted by incrementally changing the current density every 10 min at 0.1 A cm^{-2} intervals until the potential dropped below 0.2 V. In cases where a rapid decline in fuel cell potential occurred at low current density, the fuel cell was subjected to 1 L min^{-1} of air flow for 30 s to purge excess liquid water from the system before moving on to the next current density. The anode stream was directed from the upper right to the lower right corner of the MEA for the lung-inspired flow-field. The anode flow direction was reversed for the conventional double-serpentine flow-field to achieve counter-current flow orientation with air (Fig. 5). The fractal $N = 4$ flow-field was horizontally orientated as shown in Fig. 4.

2.4. Neutron imaging facility

Neutron radiography was conducted at the neutron imaging facility NEUTRA of the SINQ spallation source (Paul Scherrer Institute, PSI, Switzerland) [49]. Thermal neutrons provided by the source are extracted from a moderator tank in the thermal energy range of 1×10^{-3} to 10 eV with a Maxwellian spectrum energy of 25×10^{-3} eV. The second position was used inside the shielded area along the beam line with a maximum field-of-view of 15×15 cm^2. The fuel cell was placed in through-plane orientation to the beam to visualize liquid water across the electrode. A LiF/ZnS neutron scintillator screen converts the neutron flux of the beamline into light emission, which is then reflected by a mirror to be recorded by a CCD camera with a pixel size of 0.104 mm and a resolution of

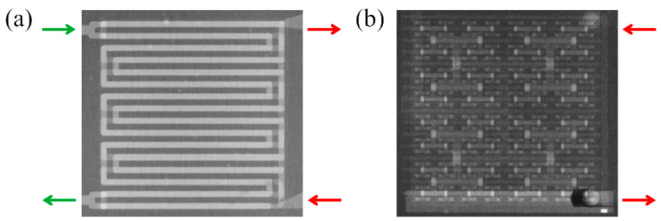

Fig. 5. Radiograph of a dry cell with (a) double-serpentine flow-field and (b) fractal flow-field with $N = 4$ branching generations. Green and red arrows indicate the flow direction of air and hydrogen, respectively. For the fractal flow-field case, air was directed perpendicular to the plane.

0.2 mm.

Images were taken with an exposure time of 20 s, which provides enough temporal resolution to capture dynamic changes in liquid water distribution during a current hold. The exposure time is within the range typically used for neutron imaging of PEMFCs (1–25 s) [43,50–52]. The intensity images are generated in FITS format, which are post-processed using PSI's in-house software written in Interactive Data Language (IDL).

2.5. Contact angle measurement

The contact angle of the fractal flow-field surface was measured using a drop shape analyser (Kruss DSA 100, Germany). An 8 μL drop of deionised water was placed on the surface of a sample and the static contact angle was measured using built-in fitting software. The 3D printed stainless steel, gold plated aluminium plate, and milled PCB surface exhibited hydrophilic surface properties with a measured contact angle of 75.3°, 81.0°, and 56.6°, respectively.

2.6. Quantification of the water thickness from neutron images

After applying necessary corrections to the resulting images (filtering, subtraction of the neutron scattering background, alignment of "operating" and reference images), images taken during cell operation were normalised to a reference image of the dry fuel cell (Fig. 5) before operation to obtain only the attenuation corresponding to the water content in the system. The thickness of water, t_{water}, is calculated from the relative neutron transmission (I/I_0) by inverting Lambert-Beer's law:

$$t_{water} = -\frac{\ln\left(\frac{I}{I_0}\right)}{\mu_{water}} \quad (1)$$

where I is the intensity of the beam in operation, I_o is the intensity of the beam for the dry fuel cell, t_{water} is the thickness of water, and μ_{water} is the attenuation coefficient of water. The attenuation coefficient of neutrons in liquid water was measured in the NEUTRA beamline for the given setup at 3.5 cm^{-1} [53]. In the following sections, the water content will be expressed as the effective water thickness in mm.

3. Results and discussion

3.1. Lung-inspired flow-field with N = 4 generations

Neutron images of the lung-inspired flow-field based PEMFC ($N = 4$) were taken during a galvanostatic operation at 0.3 A cm^{-2}. Images are displayed in chronological sequence to reveal the evolution and transport of liquid water across the channel. The blue band around the rectangular opening of the graphite sheet (red arrow in Fig. 6 (c)) is water that has penetrated into the interface between the flow-field and the graphite sheet due to incomplete sealing. The white region on the bottom right (red arrow in Fig. 6 (a)) is a result of liquid water that was present in the end-plate when the dry image was taken, but was later purged using high gas flow prior to operation.

A gradient in liquid water distribution is observed at the start of PEMFC operation with greater water content towards the bottom of the electrode. Dry hydrogen gas flows from the top to the bottom on the opposite side of the MEA, causing a portion of the liquid water generated near the top of the cathode catalyst layer to be transported across the membrane *via* back-diffusion. Water droplets appear on the channel wall as they emerge from under the land

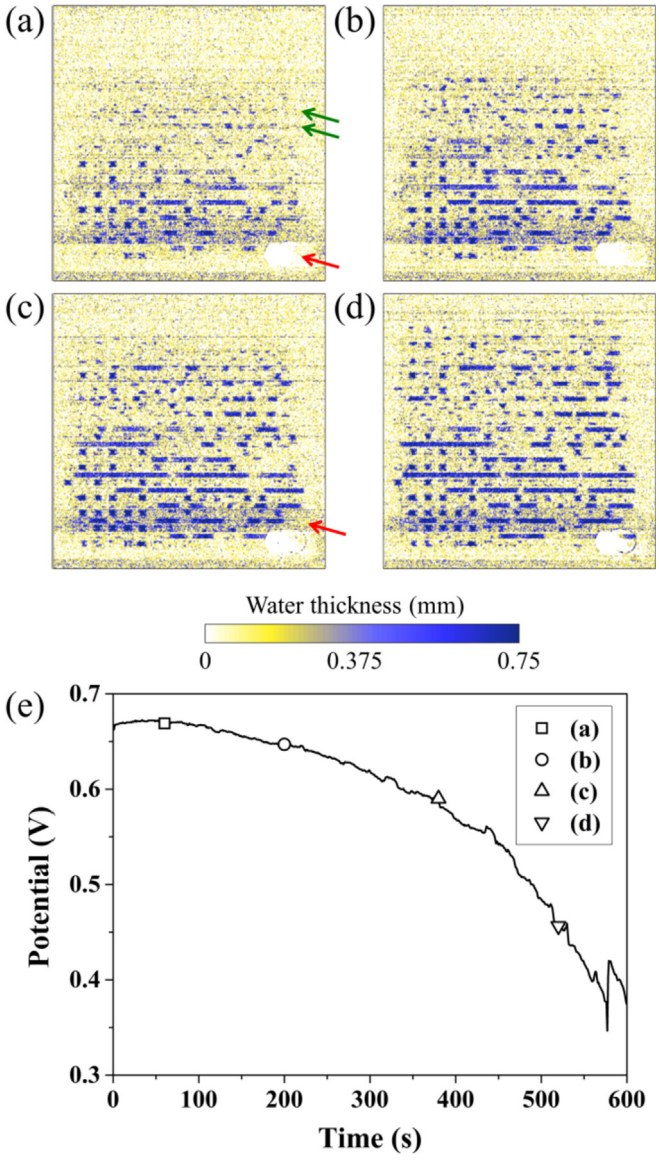

Fig. 6. (a)–(d) Neutron images showing water distribution across the lung-inspired flow-field based PEMFC with $N = 4$ at different times and (e) variation in potential during galvanostatic operation at 0.3 A cm^{-2}. The time at which each image was taken is marked on the curve.

(channels indicated with green arrows). This observation is in line with previous X-ray and neutron imaging studies showing liquid water to preferentially accumulate at the bottom of the land and start bulging into the channel once the region is saturated [32,33]. These emerged droplets grow in size and coalesce with neighbouring droplets to form slugs, causing channel blockages. The overall quantity of liquid water increases over time with significant water accumulating in the interdigitated outlet channels, which leads to an exponential decay in cell potential, as a greater region of the electrode is progressively deprived of reactant gas. This result is consistent with a previous report demonstrating flooding to occur at low current densities, caused by slow gas velocity [54]. The substantially slower gas flow across the channels of fractal flow-fields in comparison to most conventional flow-field designs makes fractal flow-fields particularly susceptible to flooding at low current density. Channel flooding in fractal flow-fields is highly undesirable, as it creates low resistance paths, redistributing the gas within the fractal distributor network, such that more gas flows

out in the vicinity of the outlet channels with less liquid water, thus starving the region underneath the flooded channels of reactant gas [55–57].

A significant portion of liquid water is found in the "inlet channels" (outlets of the fractal distributor). Since inlet gas supply is dry, all liquid water found in the inlet channels is the product of the electrochemical reaction. The generated liquid water enters the inlet channels by capillary pressure. The narrow dimensions of the final generation and the hydrophilic channel wall cause the generated liquid water to be wicked into the inlet channels. Additionally, the hydrophobic gas diffusion layer (GDL) generates capillary pressure, which forces liquid water into the channel [58–60]. We assume that these interacting forces prompt backflow of generated liquid water into the inlet channels, where gas flow is partially impeded due to minor structural imperfections within the fractal network. The finding underscores the importance of ensuring a high degree of resolution of the fractal network; this is especially so for channels in close proximity to the final generation where feature size is small, and even a minor structural defect can locally disrupt the gas distribution.

A more dynamic liquid water movement is observed across the channel at 0.5 A cm^{-2} from faster gas flow and higher channel pressure drop. Hence, flooding is substantially alleviated, as indicated by a slower decline in potential (Fig. 7; note the different scale of the Y-axis, compared to Fig. 6). The process of liquid water transport and removal is captured and highlighted with arrows.

As water droplets get expelled into the manifold (red arrow in Fig. 7 (a)), small remnants of the droplet are left behind in the channel downstream (red arrow in Fig. 7 (c)). The remnants form as a result of a breakup of the primary slug caused by the combined effects of air velocity and surface tension [61], and these exist in the form of a film [61–63]. Some liquid droplets spontaneously appear in the channel downstream, also in the form of a film (green arrows in Fig. 7 (c)). Since there was no involvement of a primary slug, we anticipate wicking of liquid water to have occurred from the hydrophobic GDL onto the hydrophilic channel wall [61,64]. Film flow allows gas to flow around it and so these droplets remain static until they grow by encountering another slug, vapor condensation or expulsion of generated liquid water from the GDL. Abrupt, temporary recovery in PEMFC potential may be indicative of liquid droplet movement across the interdigitated outlet channel into the manifold, sweeping away stationary droplets attached to the GDL and momentarily enhancing reactant transport to the catalyst layer [62,65,66].

Some liquid water droplets, on the other hand, continue to grow without advective movement (green arrows in Fig. 7 (a)). The channel pressure drop at 0.5 A cm^{-2} appears to be insufficient to remove these slugs, as larger droplets sustain greater capillary pressure (adhesive force) with the channel wall, requiring greater pressure drop for convective removal [67]. The remaining liquid droplets plug the channel of any gas flow and divert it from neighbouring inlet channels to unfilled contiguous outlet channels, resulting in inhomogeneous gas distribution and local reactant starvation [55–57].

A similar pattern emerges in the growth and discharge of liquid droplets at 0.6 A cm^{-2} (Fig. 8). The decline in potential is more pronounced, despite similar liquid water content as at 0.5 A cm^{-2}, as elevated reactant consumption rate causes greater mass transport losses within the electrode. The liquid slug of the order of the outlet channel length (red arrow in Fig. 8 (a)) starts seeping and spreading into the manifold as the channel cannot accommodate any more liquid water. The implication of excess liquid water emerging and expanding inside the manifold is significant in terms of removal of lengthy liquid slugs. As a liquid slug protrudes into the manifold, the radius of the emerging liquid expands and the

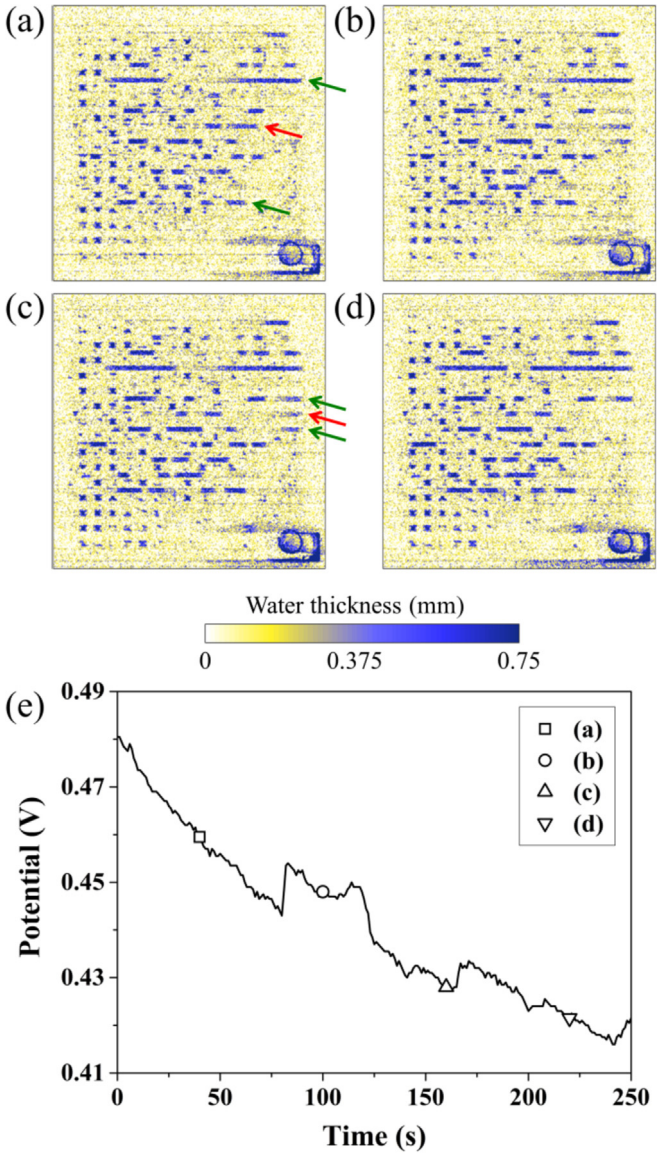

Fig. 7. (a)–(d) Neutron images showing water distribution across the lung-inspired flow-field based PEMFC with $N = 4$ at different times and (e) variation in potential during galvanostatic operation at 0.5 A cm^{-2}. The time at which each image was taken is marked on the curve.

curvature of the surface decreases. This causes a local drop in liquid pressure at the interface, inducing liquid flow in the direction of the expanding surface [58,60]. The slug is slowly pulled out of the channel in the process, as suggested by the weakening neutron signal near the channel upstream, before being completely removed. The emerged water may have joined the slug in the adjacent channel during the expansion (red arrow in Fig. 8 (c)) facilitating the removal of this slug. It is anticipated that the elevated gas pressure in the channel upstream at 0.6 A cm^{-2} also contributed to the expulsion of liquid water into the manifold. Removal of liquid water slugs is met by an instantaneous jump in the potential of over 200 mV. Such drastic performance improvement underscores the importance of maintaining outlet channels clear of liquid water in lung-inspired flow-fields for efficient and stable operation. The potential continues to gradually decline following the slug removal, due to the presence of smaller slugs across the outlet channels, which also results in lower average cell potential compared to the serpentine flow-field at the same

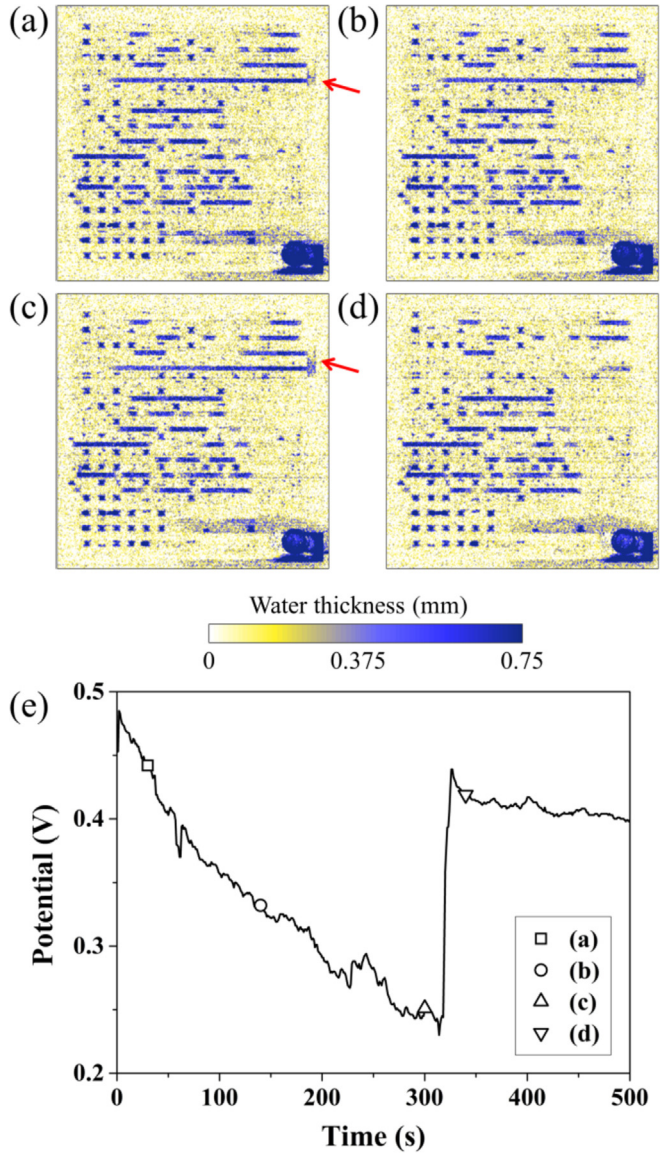

Fig. 8. (a)–(d) Neutron images showing water distribution across the lung-inspired flow-field based PEMFC with $N = 4$ generations at different times and (e) variation in potential during galvanostatic operation at 0.6 A cm^{-2}. The time at which each image was taken is marked on the curve.

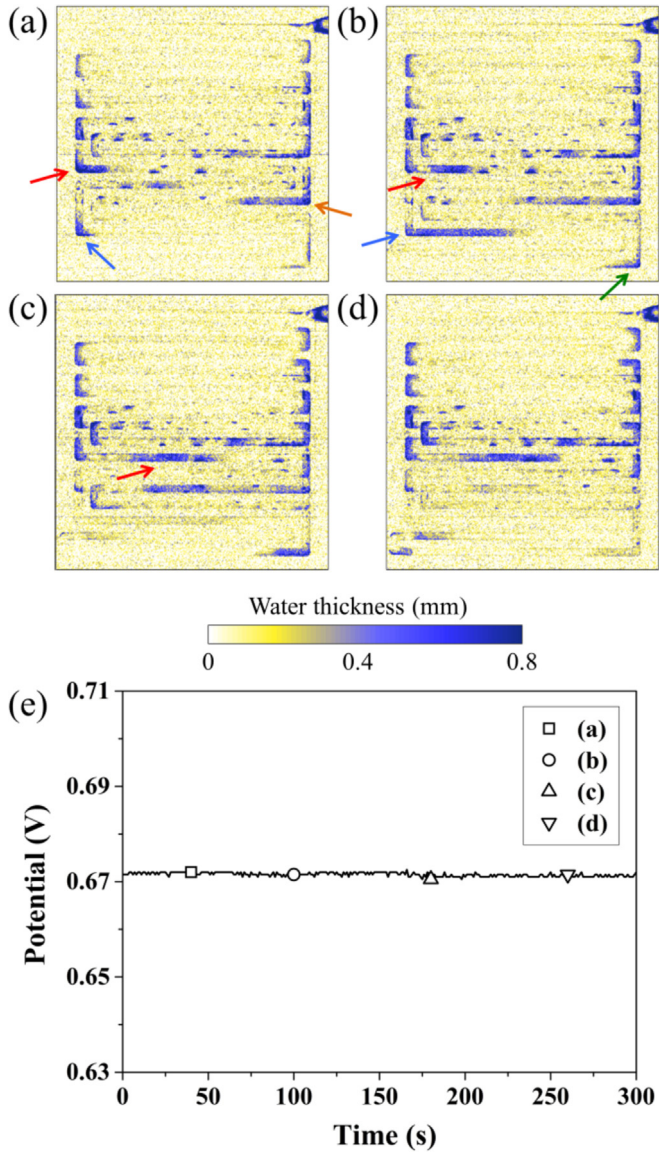

Fig. 9. (a)–(d) Neutron images showing water distribution across a conventional double-serpentine flow-field based PEMFC at different times and (e) variation in potential during galvanostatic operation at 0.3 A cm^{-2}. The time at which each image was taken is marked on the curve.

operating condition (Fig. 10). The decline is much more subtle, though, possibly as a result of alleviated flooding and no significant formation of liquid water following the slug removal; any additionally generated liquid droplets are effectively swept away by the gas flow.

3.2. Conventional double-serpentine flow-field

The water removal mechanism of a double-serpentine flow-field is assessed and compared against the fractal flow-field. The similar anode and cathode channel geometries make it difficult to distinguish the electrode to which the liquid water is associated. However, differentiation is possible with careful observation of the droplet movement and location across the electrode.

Fig. 9 shows the evolution of liquid water distribution in the channel of a conventional double-serpentine flow-field at 0.3 A cm^{-2}. The counter-current flow orientation of dry air and hydrogen causes the top and bottom region of the active area to be drier than the rest as a result of evaporation and back-diffusion, respectively. The majority of liquid water at the start of the current hold is observed in the corners of the channel in the form of droplets and film [62,68]. Liquid accumulates in corners as a result of the decreasing channel-to-channel pressure gradient near the bends [54,69,70]. Momentary changes in the neutron attenuation signal in the anode outlet manifold following the removal of these droplets at 0.6 A cm^{-2} (Fig. 10) confirms that most of these droplets are present in the anode. Liquid water in the anode remains stagnant through the current hold at 0.3 A cm^{-2} due to slow gas flow and a lack of large enough liquid droplet formation required to initiate water movement across the channel. Water droplets in the corners of the cathodic flow channel (red, blue, and orange arrows in Fig. 9) exhibit more dynamic movement and tend to spread across the channel surface in the direction of flow - a combined effect of surface hydrophilicity and faster gas flow. Some droplets (orange and blue arrows in Fig. 9 (a)) spread across the channel top

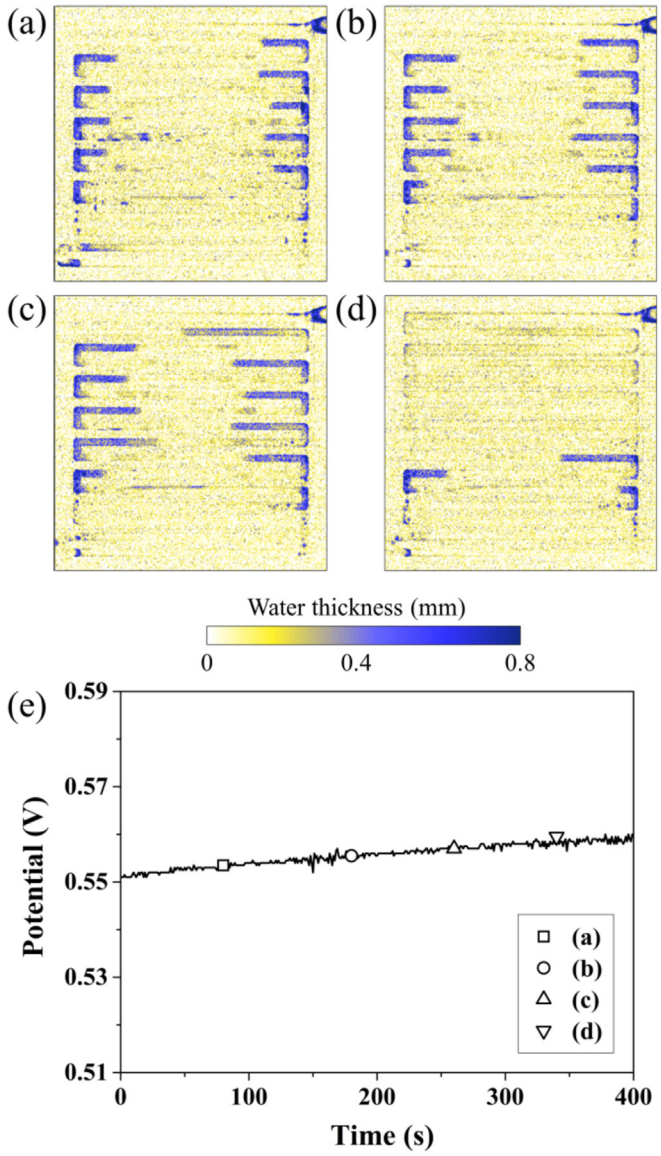

Fig. 10. (a)–(d) Neutron images showing water distribution across the double-serpentine flow-field based PEMFC at different times and (e) variation in potential during galvanostatic operation at 0.6 A cm^{-2}. The time at which each image was taken is marked on the curve.

before being discharged across the channel, sweeping away any droplets (green arrow in Fig. 9 (b)) along the way, thereby facilitating liquid water removal.

A stable PEMFC potential is recorded for the duration of the current hold in spite of fluctuating water content across the active area at 0.3 A cm^{-2}. This is ascribed to proper gas flow across the channel and cross flow created by the pressure difference between adjacent channels, allowing for convective reactant transport within the electrode. In the lung-inspired flow-field case, PEMFC performance deteriorated mainly as a result of static slugs in its interdigitated outlet channels that impeded effective reactant transport to the catalytic sites underneath. Such stagnation of water droplets does not occur for the double-serpentine flow-field because of a much lower number of channels that fosters faster gas flow and a smaller likelihood for the path of least resistance to be established between channels.

In contrast to the fractal flow-field, liquid water is observed in the anode of the serpentine flow-field based PEMFC. One plausible cause is the difference in physical properties of the channel wall. The anodic flow-fields used with the serpentine and fractal flow-fields were fabricated from PCB and aluminium plate, respectively. The contact angle of the milled PCB is significantly lower (56.6°) than that of the gold-coated aluminium plate (81°). We anticipate the higher channel surface wettability of the PCB flow-field to cause greater adherence of water to the wall, which hinders convective droplet movement across the channel, so that anodic flow channels become more susceptible to water accumulation [61,69].

Water droplets no longer emerge from the GDL onto the channel wall at 0.6 A cm^{-2} (Fig. 10). This is due to significant cross flow created by a greater pressure difference between adjacent channels, which sweeps away any generated liquid water under the land, before it accumulates and surfaces into the channel. As previously mentioned, most liquid water located in the corners is present in the anodic flow channel. Liquid water droplets in the corners gradually spread towards the centre in the direction of the hydrogen flow, before being intermittently removed (Fig. 10 (d)). The overall quantity of liquid water in the channels of the serpentine flow-field drops significantly when transitioning to a higher current density in comparison to the fractal flow-field. This is primarily due to much higher gas velocity across the channel fostering effective convective liquid water removal. This agrees well with the neutron imaging results reported by Trabold et al. that demonstrated a reduced overall quantity of water in the flow-field channels with an increase in current density due to a higher gas velocity [54]. Lastly, erratic fluctuations in potential observed with the fractal $N = 4$ flow-field at 0.6 A cm^{-2} do not occur for the double-serpentine flow-field, which corroborates the excellent water management ability of the serpentine channel geometry.

4. Conclusions

Neutron imaging has been employed to visualize liquid water distribution across lung-inspired and serpentine flow-field based PEMFCs. The serpentine flow-field based PEMFC exhibits the most stable performance as faster gas flow facilitates effective liquid water removal. On the contrary, the lung-inspired flow-field based PEMFC sustains significant liquid water accumulation in the interdigitated outlet channels, due to limited convective liquid removal from substantially slower gas flow and narrow channel dimensions, resulting in significantly higher overall water content and early onset of flooding. Flooding is alleviated at higher current densities, as faster gas flow and increased channel pressure drop yields more dynamic liquid water removal.

The importance of a well-defined, three-dimensional internal structure is identified from the observation of clogged fractal inlet channels. Any minor defects in the fractal channel network, especially in the vicinity of the final generation, render inlet channels prone to clogging with liquid water from improper gas flow.

Without condensation and channel clogging, fractal flow-fields lead to highly uniform gas transport and catalyst utilisation, and, thus, exceptional fuel cell performance [25]. However, flooding in the channels of the fractal flow-field is highly undesirable as it leads to redistribution of the gas within the fractal network, resulting in non-uniform gas distribution across the electrode, which hampers system efficiency and can potentially expedite fuel cell component degradation. Effective liquid water removal would not only reduce parasitic loads from pumping, but ensure uniform gas distribution across the active area. Implementation of the water management strategy recently developed within the group [71] into fractal flow-fields should forestall the evolution of liquid slugs in the channels, ensuring robust and reliable operation of fractal flow-field based PEMFC. However, such mechanism requires the integration of

water transport channels adjacent to land, and interdigitated outlet channels of the fractal flow-fields with a wall thickness of ≤0.5 mm. Such intricate design requirement calls for a careful consideration of build orientation, laser parameters, and possible modification to the channel geometry to prevent the wall (between gas and water transport channels) from collapsing during laser sintering.

Acknowledgement

The authors gratefully acknowledge the financial support from an EPSRC “Frontier Engineering” Award (EP/K038656/1) and a UCL Faculty of Engineering Sciences Dean's Scholarship for Jason I. S. Cho. The authors would also like to acknowledge the EPSRC for supporting the Electrochemical Innovation Lab through EP/M009394/1, EP/G030995/1, EP/I037024/1, EP/M014371/1 and EP/M023508/1, and the Royal Academy of Engineering for supporting Paul R. Shearing. The authors would also like to thank Dr Dimitrios Tsaoulidis for the demonstration of the drop shape analyser.

References

[1] White RT, Orfino FP, Hannach ME, Luo O, Dutta M, Young AP, Kjeang E. J Electrochem Soc 2016;163:F1337–43.
[2] Barbir F. CHAPTER 2 - fuel cell basic chemistry and thermodynamics. In: Barbir F, editor. PEM fuel cells. Burlington: Academic Press; 2005. p. 17–32.
[3] Li X, Sabir I. Int J Hydrogen Energy 2005;30:359–71.
[4] Ramos-Alvarado B, Hernandez-Guerrero A, Elizalde-Blancas F, Ellis MW. Int J Hydrogen Energy 2011;36:12965–76.
[5] Liu H, Li P, Juarez-Robles D, Wang K, Hernandez-Guerrero A. Front Energy Res 2014;2.
[6] Wang J, Wang H. Fuel Cell 2012;12:989–1003.
[7] Wang J. Appl Energy 2015;157:640–63.
[8] Arvay A, French J, Wang JC, Peng XH, Kannan AM. Int J Hydrogen Energy 2013;38:3717–26.
[9] Wu Y, Cho JIS, Neville TP, Meyer Q, Zeische R, Boillat P, Cochet M, Shearing PR, Brett DJL. J Power Sources 2018;399:254–63.
[10] C. Wang, Q. Zhang, S. Shen, X. Yan, F. Zhu, X. Cheng, J. Zhang, 7 (2017) 43447.
[11] Shimpalee S, Hirano S, DeBolt M, Lilavivat V, Weidner JW, Khunatorn Y. J Electrochem Soc 2017;164:E3073–80.
[12] Esfeh HK, Azarafza A, Hamid MKA. RSC Adv 2017;7:32893–902.
[13] Jeon DH, Greenway S, Shimpalee S, Van Zee JW. Int J Hydrogen Energy 2008;33:1052–66.
[14] Sasmito AP, Kurnia JC, Mujumdar AS. Energy 2012;44:278–91.
[15] Das PK, Li X, Liu Z-S. Int J Hydrogen Energy 2010;35:2403–16.
[16] Li H, Tang Y, Wang Z, Shi Z, Wu S, Song D, Zhang J, Fatih K, Zhang J, Wang H, Liu Z, Abouatallah R, Mazza A. J Power Sources 2008;178:103–17.
[17] Zhang G, Shen S, Guo L, Liu H. Int J Hydrogen Energy 2012;37:1884–92.
[18] Jung J, Park B, Kim J. Nanoscale Res Lett 2012;7:34.
[19] Taniguchi A, Akita T, Yasuda K, Miyazaki Y. Int J Hydrogen Energy 2008;33:2323–9.
[20] Chen T, Xiao Y, Chen T. Energy Procedia 2012;28:134–9.
[21] Kloess JP, Wang X, Liu J, Shi Z, Guessous L. J Power Sources 2009;188:132–40.
[22] Damian-Ascencio CE, Saldaña-Robles A, Hernandez-Guerrero A, Cano-Andrade S. Energy 2017;133:306–16.
[23] Withers P. J Herpetol 1993;27:265–70.
[24] Comanns P, Buchberger G, Buchsbaum A, Baumgartner R, Kogler A, Bauer S, Baumgartner W. J R Soc Interface 2015;12.
[25] Trogadas P, Cho JIS, Neville TP, Marquis J, Wu B, Brett DJL, Coppens MO. Energy Environ Sci 2018;11:136–43.
[26] Aslam RM, Ingham DB, Ismail MS, Hughes KJ, Ma L, Pourkashanian M. J Energy Inst 2017;91:1057–70.
[27] Inman K, Wang X. Int J Hydrogen Energy 2014;39:19691–700.
[28] Bozorgnezhad A, Shams M, Kanani H, Hasheminasab M, Ahmadi G. Int J Hydrogen Energy 2016;41:19164–81.
[29] Alrwashdeh SS, Manke I, Markötter H, Klages M, Göbel M, Haußmann J, Scholta J, Banhart J. ACS Nano 2017;11:5944–9.
[30] Eller J, Rosén T, Marone F, Stampanoni M, Wokaun A, Büchi FN. J Electrochem Soc 2011;158:B963–70.
[31] Hinebaugh J, Lee J, Mascarenhas C, Bazylak A. Electrochim Acta 2015;184:417–26.
[32] Chevalier S, Ge N, Lee J, George MG, Liu H, Shrestha P, Muirhead D, Lavielle N, Hatton BD, Bazylak A. J Power Sources 2017;352:281–90.
[33] Meyer Q, Ashton S, Boillat P, Cochet M, Engebretsen E, Finegan DP, Lu X, Bailey JJ, Mansor N, Abdulaziz R, Taiwo OO, Jervis R, Torija S, Benson P, Foster S, Adcock P, Shearing PR, Brett DJL. Electrochim Acta 2016;211:478–87.
[34] Meyer Q, Ashton S, Torija S, Gurney C, Boillat P, Cochet M, Engebretsen E, Finegan DP, Adcock P, Shearing PR, Brett DJL. Electrochim Acta 2016;203:198–205.
[35] Murakawa H, Sugimoto K, Kitamura N, Sawada M, Asano H, Takenaka N, Saito Y. Phys Procedia 2015;69:607–11.
[36] Tsushima S, Teranishi K, Hirai S. Electrochem Solid State Lett 2004;7:A269–72.
[37] Minard KR, Viswanathan VV, Majors PD, Wang L-Q, Rieke PC. J Power Sources 2006;161:856–63.
[38] Zhang Z, Martin J, Wu J, Wang H, Promislow K, Balcom BJ. J Magn Reson 2008;193:259–66.
[39] Iranzo A, Boillat P, Biesdorf J, Salva A. Energy 2015;82:914–21.
[40] Alrwashdeh SS, Markötter H, Haußmann J, Arlt T, Klages M, Scholta J, Banhart J, Manke I. Energy 2016;102:161–5.
[41] Salva JA, Iranzo A, Rosa F, Tapia E. Energy 2016;101:100–12.
[42] Boillat P, Lehmann EH, Trtik P, Cochet M. Curr Opin Electrochem 2017;5:3–10.
[43] Iranzo A, Boillat P, Oberholzer P, Guerra J. Energy 2014;68:971–81.
[44] Hickner M, Hussey D. Neutron radioscopy: industrial and scientific applications. 2010.
[45] Mukundan R, Borup RL. Fuel Cell 2009;9:499–505.
[46] Oberholzer P, Boillat P, Siegrist R, Perego R, Kästner A, Lehmann E, Scherer GG, Wokaun A. J Electrochem Soc 2011;159:B235–45.
[47] LaManna JM, Chakraborty S, Gagliardo JJ, Mench MM. Int J Hydrogen Energy 2014;39:3387–96.
[48] Meyer Q, Mansor N, Iacoviello F, Cullen PL, Jervis R, Finegan D, Tan C, Bailey J, Shearing PR, Brett DJL. Electrochim Acta 2017;242:125–36.
[49] Lehmann EH, Vontobel P, Wiezel L. Nondestr Test Eval 2001;16:191–202.
[50] Meyer Q, Ashton S, Jervis R, Finegan DP, Boillat P, Cochet M, Curnick O, Reisch T, Adcock P, Shearing PR, Brett DJL. Electrochim Acta 2015;180:307–15.
[51] Boillat P, Oberholzer P, Kaestner A, Siegrist R, Lehmann EH, Scherer GG, Wokaun A. J Electrochem Soc 2012;159:F210–8.
[52] Murakawa H, Sugimoto K, Miyata K, Asano H, Takenaka N, Saito Y. Phys Procedia 2013;43:277–81.
[53] Iranzo A, Boillat P. Int J Hydrogen Energy 2014;39:17240–5.
[54] Trabold TA, Owejan JP, Jacobson DL, Arif M, Huffman PR. Int J Heat Mass Tran 2006;49:4712–20.
[55] Kandlikar SG, Lu Z, Domigan WE, White AD, Benedict MW. Int J Heat Mass Tran 2009;52:1741–52.
[56] Ji M, Wei Z. Energies 2009;2:1057.
[57] Jiao K, Zhou B, Quan P. J Power Sources 2006;157:226–43.
[58] Litster S, Sinton D, Djilali N. J Power Sources 2006;154:95–105.
[59] Nam JH, Kaviany M. Int J Heat Mass Tran 2003;46:4595–611.
[60] Quesnel C, Cao R, Lehr J, Kietzig A-M, Weber AZ, Gostick JT. J Phys Chem C 2015;119:22934–44.
[61] Lorenzini-Gutierrez D, Kandlikar SG, Hernandez-Guerrero A, Elizalde-Blancas F. J Power Sources 2015;279:567–80.
[62] Spernjak D, Prasad AK, Advani SG. J Power Sources 2007;170:334–44.
[63] Cheah MJ, Kevrekidis IG, Benziger JB. Langmuir 2013;29:9918–34.
[64] Zhang FY, Yang XG, Wang CY. J Electrochem Soc 2006;153:A225–32.
[65] Hickner MA, Siegel NP, Chen KS, Hussey DS, Jacobson DL. J Electrochem Soc 2010;157:B32–8.
[66] Spernjak D, Prasad AK, Advani SG. J Power Sources 2010;195:3553–68.
[67] Bachman J, Charvet M, Santamaria A, Tang H-Y, Park JW, Walker R. Int J Hydrogen Energy 2012;37:17172–9.
[68] Jo JH, Kim WT. Int J Hydrogen Energy 2015;40:8368–83.
[69] Ferreira RB, Falcão DS, Oliveira VB, Pinto AMFR. Appl Energy 2017;203:474–95.
[70] Suresh PV, Jayanti S, Deshpande AP, Haridoss P. Int J Hydrogen Energy 2011;36:6067–72.
[71] Cho JIS, Neville TP, Trogadas P, Bailey J, Shearing P, Brett DJL, Coppens MO. Int J Hydrogen Energy 2018;43:21949–58.